Measuring μ distortions from the thermal Sunyaev-Zeldovich effect

David Zegeye,[1,2] Thomas Crawford,[1,2] and Wayne Hu[1,2,3]

[1]Department of Astronomy and Astrophysics, The University of Chicago, Chicago, Illinois 60637, USA
[2]Kavli Institute for Cosmological Physics, The University of Chicago, Chicago, Illinois 60637, USA
[3]Enrico Fermi Institute, The University of Chicago, Chicago, Illinois 60637, USA

(Received 31 July 2023; accepted 16 January 2024; published 4 March 2024)

The thermal Sunyaev-Zeldovich (tSZ) effect is a spectral distortion of the cosmic microwave background (CMB) resulting from inverse Compton scattering of CMB photons with electrons in the medium of galaxy clusters. The spectrum of the tSZ effect is typically calculated assuming the spectrum of the CMB is a blackbody. However, energy or photon number injection at any epoch after photon creation processes become inefficient will distort the blackbody, potentially leading to a chemical potential or μ distortion for early injection. These *primordial* spectral distortions will therefore introduce a change in the tSZ effect, effectively a distortion of a distortion. While this effect is small for an individual cluster's spectrum, upcoming and proposed CMB surveys expect to detect tens of thousands of clusters with the tSZ effect. In this paper, we forecast constraints on the μ-distortion monopole from the distortion of the tSZ spectrum of clusters measured by CMB surveys. We find that planned experiments have the raw sensitivity to place constraints on μ that are comparable to or better than existing constraints but control over foregrounds and other systematics will be critical.

DOI: 10.1103/PhysRevD.109.063503

I. INTRODUCTION

The cosmic microwave background (CMB) provides us with vital information about the origin and evolution of our observable Universe and of the underlying physical laws that govern it. We have greatly improved measurements of CMB temperature and polarization anisotropy over the last 20 years with experiments such as WMAP [1] and Planck [2].

On the other hand, our constraints on the frequency spectrum of the CMB have not improved since the measurements of the Far Infrared Absolute Spectrophotometer on the Cosmic Background Explorer (COBE/FIRAS hereafter) [3]. Although the measured CMB spectrum closely matches a blackbody, the CMB in fact is expected to have some small distortion away from a blackbody spectrum.

Energy injections in the form of diffusion damping of small-scale anisotropies, resulting from imperfect photon-baryon coupling in the prerecombination plasma, during periods of inefficient thermalization ($z \lesssim 2 \times 10^6$) will slightly distort the spectrum. For $2 \times 10^6 \gtrsim z \gtrsim 5 \times 10^4$, distortions of the μ type are generated by this process, while for $5 \times 10^4 \gtrsim z \gtrsim 1100$ distortions of the y type are generated. Using an internal blackbody as a calibrator, COBE/FIRAS was able to confirm the CMB spectrum closely follows a blackbody distribution and place upper limits of $|y| < 1.5 \times 10^{-5}$ and $|\mu| < 9 \times 10^{-5}$ (95% C.L.) (see also follow-up analyses [4,5]).

While diffusion damping of fluctuations from slow-roll inflation is one small ($\mu \gtrsim 10^{-8}$) but guaranteed method for generating spectral distortions before recombination [6–9], other possibilities include annihilating particles [10], diffusion damping in inflationary models that generate primordial black holes [11], primordial black hole evaporation [12], and primordial gravitational waves [13].

The CMB radiation can also be distorted by postrecombination sources, for example through inverse Compton scattering off of the hot electron gas in galaxy clusters, resulting in cluster-scale distortions of the CMB spectrum, a phenomenon referred to as the thermal Sunyaev-Zeldovich (tSZ) effect [6]. In general, spectral distortions allow one to probe any process associated with energy injection into the CMB after the thermalization epoch.

Measuring the mean, or monopole, frequency spectrum of the CMB is extremely challenging, because it requires an experiment to retain information about the absolute power received from the sky, not just the difference in power between different sky locations. Absolute measurements require exquisite stability over long timescales and tight control over any spatially varying sources of emission. Note that these stability requirements remain even for an experiment that does not require an overall absolute gain calibration (e.g., [14,15]). For these reasons, it is often assumed that such measurements can only be made from space.

One way around these requirements is to measure the mean distortion of an anisotropic signal that can be measured

differentially, such as the CMB dipole [16] or primary CMB anisotropy. The issue with using CMB temperature anisotropy is that most differential CMB experiments use the temperature anisotropy (either the dipole—or, more precisely, the annual modulation of the dipole—or the degree-scale and smaller anisotropy) as a calibration source, with the underlying assumption that the photon distribution follows a perfect blackbody. This effectively destroys any sensitivity to spectral distortions from the dipole or primary anisotropy, because the calibrated spectrum of the anisotropy will be forced to look like the derivative of a blackbody. Put another way, experiments designed to measure spectral distortions in the dipole or primary CMB anisotropy must find a different way of calibrating the relative response between observing frequencies.

In this work, we investigate the prospect for using the tSZ effect to measure monopole spectral distortions. This method, first proposed by [17], was used recently by [18] to forecast constraints on the (primordial) y distortion of the CMB from distortions of the (local-universe) tSZ effect. As discussed in [19], this technique can in principle be applied to y- or μ-type distortions and was also proposed in [20] to test the validity of early measurements indicating large spectral distortions near the blackbody peak, later demonstrated by COBE/FIRAS to be spurious. Similar works have explored constraining the primordial recombination radiation [21] and the redshift evolution of the CMB temperature from the distortion of the tSZ effect. This paper focuses on the potential constraints on the mean value of μ-type distortions from measurements of the tSZ effect in the direction of massive clusters of galaxies using calibration from primary CMB temperature anisotropy under the blackbody assumption. We will forecast constraints on this quantity from the upcoming CMB-S4 experiment [22] as well as one based on the proposed CMB-HD experiment [23].

II. CMB SPECTRAL DISTORTIONS

A. μ and y distortions

At early epochs, any changes in the photon phase space distribution f are efficiently thermalized to a blackbody distribution through the joint action of the photon-number-changing processes double Compton scattering and bremsstrahlung and the energy-exchanging process (single) Compton scattering. Number-changing processes fall out of equilibrium at a redshift $z_i \sim 2 \times 10^6$ after which the photon distribution evolves mainly under the Kompaneets equation [24] (see Appendix B for relativistic corrections)

$$\frac{\partial f}{\partial \tau} = \frac{k_B T_e}{m_e c^2} \frac{1}{x_e^2} \frac{\partial}{\partial x_e} \left[x_e^4 \left(\frac{\partial f}{\partial x_e} + f(1+f) \right) \right], \tag{1}$$

where τ is the Thomson optical depth and $x_e = h\nu/k_B T_e$ for a thermal distribution of electrons at temperature T_e. The equilibrium distribution under the Kompaneets equation is a Bose-Einstein distribution. Any changes to the number or energy density of the photons thereafter lead to a μ-type distortion

$$f = (e^{x+\mu} - 1)^{-1}, \tag{2}$$

where $x = h\nu/k_B T$ with the temperature of the photons $T = T_e$. For example, a fractional energy injection of $\Delta\rho/\rho$ to the photons leads to $\mu \sim 1.4\Delta\rho/\rho$. Energy exchange via Compton scattering falls out of equilibrium at around $z_f \sim 5 \times 10^4$. After this epoch, we can solve the Kompaneets equation by plugging the unperturbed spectrum (2) into the right-hand side of Eq. (1) and integrating [19]

$$\Delta f(x, \mu, y) = \int d\tau \frac{\partial f}{\partial \tau} \approx yx e^{x+\mu} f^2 g(x, \mu), \tag{3}$$

with

$$g(x, \mu) = x \coth\left(\frac{x+\mu}{2} \right) - 4, \tag{4}$$

where the Comptonization parameter

$$y = \int d\tau \frac{k_B (T_e - T)}{m_e c^2} \tag{5}$$

is assumed to be $|y| \ll 1$. This generalizes the standard expression for the y-type distortion to the case where $\mu \neq 0$; i.e., the photons possess an initial μ-type distortion. Notice that the spectrum only changes when $T_e \neq T$, e.g., when the electrons are heated after z_f. In particular, we are interested in the case where the hot electrons exist in galaxy clusters and produce the late-time y-type distortions known as the tSZ effect. Our generalization implies that in principle the initial μ value can be determined from a precise measurement of the tSZ spectrum.

B. Interfrequency calibration

As discussed in Sec. I, most differential CMB experiments derive their interfrequency calibration from CMB anisotropy, either the CMB dipole or the primary temperature anisotropy, under the assumption that the background photon distribution is a pure blackbody. Experiments that have access to very large angular scales, such as the *Planck* and *WMAP* satellites, calibrate off of the annual modulation of the dipole from Earth's motion around the Sun. When compared to predictions using our precise knowledge of the current CMB temperature T_0 and Earth's orbital velocity, and assuming a blackbody background, this provides both an interfrequency calibration and a calibration of the overall intensity scale. Experiments that use the primary anisotropy for interfrequency calibration (as is the case for most

ground-based CMB experiments) need a separate reference for the absolute intensity scale, but since the inference for μ depends on the relative frequency dependence for a given amplitude y, an accurate relative calibration of channels is more important than the overall absolute calibration. For the specific measurement envisioned in this work, the absolute scale is effectively marginalized over, and we neglect it hereafter.

In practice, for the case of calibration off of the annual modulation of the dipole, the signal in each frequency band is scaled to agree with predictions assuming a pure blackbody background. The situation is similar for calibration off of the primary anisotropy: Maps at every observing frequency ν are compared to each other in a region of the sky and a range of angular scales in which the primary CMB anisotropy is the dominant signal, and the maps are calibrated so that the signal follows the expected spectrum of temperature fluctuations in a background blackbody with mean temperature T_0. In both cases, the true spectrum of the calibration source is that of temperature fluctuations in the true background, and the result of calibrating assuming a blackbody background is that the measured, calibrated dipole and/or primary CMB anisotropy is forced to follow the spectrum of temperature fluctuations in a blackbody.

Let us examine the case of calibrating off of the observed dipole in the presence of a monopole μ distortion in the background spectrum while assuming the background spectrum is a blackbody. (The results in the case of calibrating off of the primary CMB anisotropy are identical.) In the case of dipole calibration, the Lorentz invariance of f implies that the specific intensity in the boosted frame $I_\nu^d \propto \nu^3 f$ obeys

$$I_\nu^d \propto \frac{\nu^3}{e^{h\nu_{\rm rest}/k_B T+\mu}-1}, \tag{6}$$

where

$$\nu_{\rm rest} = \left(\frac{1-\beta\cos\theta}{\sqrt{1-\beta^2}}\right)\nu \tag{7}$$

and θ is the angle between the line of sight and the velocity. Notice that we can absorb the Doppler shift into a temperature anisotropy as usual and to first order in β, $T(\theta) \approx T(1+\beta\cos\theta)$. The change in the specific intensity becomes

$$\Delta I_\nu^d \approx (\beta\cos\theta) T \frac{\partial I_\nu}{\partial T}. \tag{8}$$

The frequency dependence involves the derivative of I_ν, and this result holds for calibration involving any type of temperature anisotropy by suitably generalizing the anisotropy source, not just a dipole due to a boost. Note that we are ignoring higher-order terms in the expansion of the blackbody fluctuation spectrum, which are negligible at least for the order 10^{-5} anisotropy in the CMB.

If a blackbody background distribution is assumed in the calibration process, then the anisotropy-calibrated specific intensity I_ν^c differs from the true specific intensity I_ν by

$$I_\nu^c = C(x,\mu) I_\nu, \tag{9}$$

where the miscalibration from the true spectrum is characterized as

$$C(x,\mu) = \frac{\partial B_\nu/\partial T}{\partial I_\nu/\partial T}. \tag{10}$$

Notice that this anisotropy calibration factor involves the spectral shape of the derivative of the specific intensity, not the specific intensity itself. Thus, while this particular calibration procedure removes any information about spectral distortions from the primary anisotropy signal, distortions of signals that do not have the spectrum of the temperature derivative of the CMB monopole spectrum can still be measured.

Counterintuitively, this observability includes the μ distortion of the CMB monopole itself:

$$\frac{I_\nu^c(\mu)}{B_\nu} = \frac{I_\nu}{B_\nu}\frac{\partial B_\nu/\partial T}{\partial I_\nu/\partial T} = e^{-\mu}\frac{e^{x+\mu}-1}{e^x-1}, \tag{11}$$

and the correction for $|\mu| \ll x \ll 1$ goes as μ/x. In practice, as discussed in Sec. I, since this measurement requires a nondifferential measurement on the sky, it remains challenging from the ground.

Now let us apply this sort of calibration to the tSZ distortion of a μ-distorted background in the direction of a galaxy cluster, a signal which can be measured differentially. In terms of the calibrated apparent CMB temperature fluctuation at frequency ν, ΔT, we obtain

$$\begin{aligned}\Delta T(x,\mu) &\equiv \frac{\Delta I_\nu^c}{\partial B_\nu/\partial T} = \frac{\Delta I_\nu}{\partial I_\nu/\partial T} = \frac{\Delta f}{\partial f/\partial T} \\ &= y T_0 g(x,\mu),\end{aligned} \tag{12}$$

where we have used Eq. (3) for Δf. Notice that the anisotropy calibrated ΔT differs from the absolutely calibrated temperature fluctuation, and Eq. (4) for $g(x,\mu)$ carries the measurable frequency dependence under anisotropy calibration. This difference is illustrated in Fig. 1. Notice also that in both cases the response to μ increases at low frequency but with the opposite sign.

C. Cluster model

Using Eq. (5), our model for the value of the Compton y parameter in the direction of an isothermal cluster ($T_e = \text{const} \gg T$) is

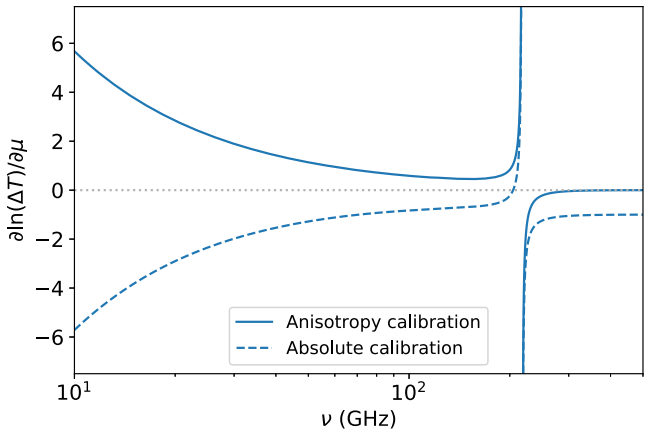

FIG. 1. The fractional response of the tSZ temperature spectrum $\partial \ln \Delta T/\partial\mu$ to a monopole μ distortion with anisotropy calibration as we assume in this work (solid blue line $\partial \ln g/\partial\mu$) vs absolute calibration [dashed blue line $\partial \ln(g/C)/\partial\mu$]. The dotted gray line denotes an undistorted spectrum for reference and the spike in the curves occurs at the tSZ null where the *fractional* response diverges corresponding to a finite change in the location of the null.

$$y(\theta) = \frac{k_B T_e}{m_e c^2}\tau(\theta), \tag{13}$$

where θ is the angular distance from the center of the cluster. For the optical depth profile $\tau(\theta)$ we follow e.g., [25], and adopt a spherically symmetric β model or King profile with $\beta = 1$ and express Eq. (13) as

$$y(\theta) = y_c\left[1 + \left(\frac{\theta}{\theta_c}\right)^2\right]^{-1}. \tag{14}$$

Here, the angular size of the cluster's core is given by $\theta_c = r_c/D_A$, with D_A being the angular diameter distance and r_c the core radius of the cluster, all in comoving coordinates for later convenience. We follow [26,27] and we adopt the relation $r_c \sim 0.2R_{500c}$, where R_{500c} is the radius at which the enclosed spherically averaged density is 500 times the critical density $\rho_c(z) \equiv 3H^2(z)/8\pi G$.

For y_c we adopt the self-similar scaling relation

$$y_c = A\tilde{E}^2(z)\left(\frac{M_{500c}}{10^{14}M_\odot}\right), \tag{15}$$

where

$$\tilde{E}(z) \equiv \frac{H(z)}{70\ \mathrm{km/s/Mpc}} \tag{16}$$

and the normalization A from x-ray cluster observations of luminosity and temperature at low z [28] to calibrate the universal pressure profile [Eq. (6) in Ref. [29]]

$$A = 0.97 \times 10^{-5} h^{-3/2}. \tag{17}$$

Note using this normalization in the context of Eq. (14) is approximate given differences with the universal pressure profile [30]. We also adopt the temperature-mass relation [31]

$$k_B T_e = 2.28\left(\frac{M_{500c}}{10^{14}M_\odot}\tilde{E}(z)\right)^{0.585}\ \mathrm{keV}. \tag{18}$$

Because the noise in our forecasted surveys is expected to be diagonal in spherical harmonic (ℓ, m) space, we choose to work in that basis. To transform Eq. (14) into ℓ, m space, we note that since even the most massive and low-redshift clusters only subtend a small angle on the sky, we can use the flat-sky approximation. As detailed in Appendix A, in coordinates centered on the cluster at $\theta = 0$, the spherical harmonic-space cluster profile is given by

$$y_{\ell m} = \sqrt{\frac{2\ell+1}{4\pi}}\delta_{m,0}y(\ell), \tag{19}$$

where

$$y(\ell) = y_c 2\pi\theta_c^2 K_0(\ell\theta_c) \tag{20}$$

and $K_n(x)$ is the modified Bessel function of the second kind.

III. FORECAST

A. Survey specifications

We forecast our constraints on μ from tSZ cluster measurements using instrument configurations based on the upcoming CMB-S4 experiment and the proposed CMB-HD experiment. CMB-S4 will conduct two surveys: The wide survey conducted from Chile will cover 67% of the sky, while the deep survey will concentrate a similar amount of total observing weight on 3% of the sky from the South Pole. From here on, we will refer to these two CMB-S4 surveys as "S4-wide" and "S4-deep," respectively. Both surveys will have similar beam sizes and differ mainly in the noise in the sky maps. The CMB-HD-like survey we forecast for here covers 50% of the sky. For all three surveys, we use the instrument configuration parameters from Table 1 of [32], which we reproduce in Table I. We note that for both S4-wide and CMB-HD, the galactic plane will significantly contaminate our maps of tSZ clusters and reduce our ability to accurately measure the cluster spectrum. Therefore, for these surveys we assume $f_{\mathrm{sky}} = 0.5$.

B. Cluster catalog

In addition to specifications on map noise, angular resolution, and sky fraction, to forecast constraints on μ from the distortion of the tSZ spectrum we also need to

TABLE I. Specifications for the CMB-S4 wide and deep surveys and a CMB-HD-like survey, taken from [32].

Channels (GHz)		30	40	90	150	220	270
Survey	$f_{\rm sky}$	$\theta_{\rm FWHM}$ & $\sqrt{C_{\rm w}}$ (μK-arcmin)					
S4-wide	50%	7.3′	5.5′	2.3′	1.5′	1.0′	0.8′
		21.8	12.4	2.0	2.0	6.9	16.7
S4-deep	3%	8.4′	5.8′	2.5′	1.6′	1.1′	1.0′
		4.6	2.94	0.45	0.41	1.29	3.07
CMB-HD	50%	1.4′	1.05′	0.45′	0.25′	0.2′	0.15′
		6.5	3.4	0.73	0.79	2.0	2.7

define a sample of galaxy clusters. For each of the three surveys considered here, we use the expected cluster catalog for that survey, based on work from [32,33].

Underlying the expected number of clusters detected by a given CMB experiment is the halo mass function $dn/d\ln M$, the number density of host dark matter halos at a given redshift z over a logarithmic mass interval $d\ln M$. We adopt for this quantity the Tinker mass function [34] as implemented in the publicly available code Colossus [35,36]. Our cosmological parameters are taken from Planck 2018 [2], where $\Omega_m = 1 - \Omega_\Lambda = 0.31$, $\Omega_b = 0.049$, $H_0 = 67.7$ km/s/Mpc, $\sigma_8 = 0.81$, $\tau = 0.054$, and $n_s = 0.965$.

A given experiment will have a selection function in mass and redshift which we approximate here as a simple mass limit as a function of redshift $M_{\rm lim}(z)$. For each of the three surveys we forecast, we use the values of $M_{\rm lim}(z)$ calculated in [32]. These limits are reproduced in Fig. 2. The jaggedness of the curves reflects the $\Delta z = 0.1$ binning in Ref. [32] as does our effective $z_{\rm min} = 0.05$, but we will show in later sections that this effective redshift limit does not affect our results significantly. The general trend of the $M_{\rm lim}(z)$ curves—which is the opposite of mass-limit curves from, e.g., x-ray-selected cluster samples—is discussed in Sec. 3.2.1 of [33].

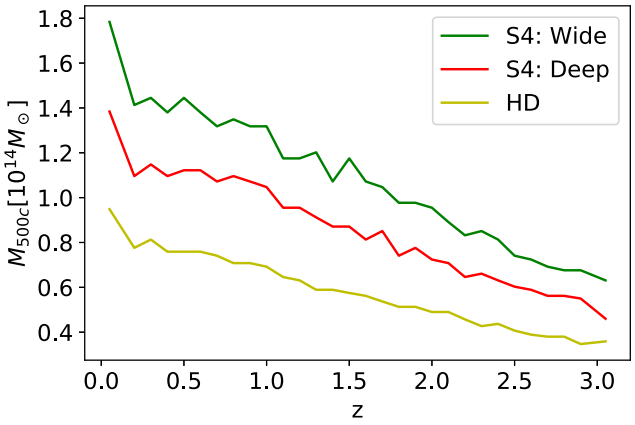

FIG. 2. The mass detection limit $M_{\rm lim}$ as a function of redshift from Ref. [32], linearly interpolated between their $\Delta z = 0.1$ bins.

We model the expected number of total detected clusters for each survey as

$$N_{\rm tot} = 4\pi f_{\rm sky} \int_{z_{\rm min}}^{\infty} dz \frac{D_A^2(z)}{H(z)} \int_{M_{\rm lim}(z)}^{\infty} \frac{dM}{M} \frac{dn}{d\ln M}, \quad (21)$$

where $f_{\rm sky}$ is the fraction of sky measured by the experiment. We find that for our fiducial cosmology: $N_{\rm tot} = 1.04 \times 10^5$ for S4-wide; 1.10×10^4 for S4-deep, and 4.63×10^5 for CMB-HD. Our number of clusters agrees with [32] to within ∼3% for S4-wide, ∼7% for S4-deep, and ∼10% for CMB-HD.

C. Forecasting method

We forecast constraints on μ from the distorted tSZ spectrum in the direction of massive clusters using a Fisher matrix technique. First, we define the likelihood per cluster in the catalog. Given the expression for the measured, calibrated tSZ spectrum from Eq. (12), we model the cluster likelihood $\mathcal{L}$ as

$$-2\ln\mathcal{L} = \sum_{ij,\ell m,\ell' m'} \left[\Delta T_{i,\ell m} - y_{\ell m} T_0 g(x_i,\mu)\right] \times \mathbf{C}^{-1}_{ij,\ell m \ell' m'} \left[\Delta T_{j,\ell' m'} - y_{\ell' m'} T_0 g(x_j,\mu)\right], \quad (22)$$

where i and j run over frequency bands, $\Delta T_{i,\ell m}$ is the measured, calibrated (spherical harmonic-space) temperature fluctuation in band i in the direction of the cluster, $y_{\ell m}$ is the spherical harmonic-space cluster profile, and we have approximated the sources of noise as Gaussian by characterizing the likelihood with the covariance matrix $\mathbf{C}$. Using Eq. (20) for the cluster profile and assuming statistical isotropy, there is no azimuthal dependence in the model or the covariance, and the covariance will be diagonal in ℓ, in which case we can write

$$-2\ln\mathcal{L} = \sum_{ij,\ell} \frac{2\ell+1}{4\pi} \left[\Delta T_{i,\ell} - y(\ell) T_0 g(x_i,\mu)\right] \times (\mathbf{C}_\ell)^{-1}_{ij} \left[\Delta T_{j,\ell} - y(\ell) T_0 g(x_j,\mu)\right]. \quad (23)$$

For the noise covariance matrix, we begin with a baseline of just uncorrelated white noise and write

$$(\mathbf{C}_\ell)_{ij} \to (\mathbf{C}_\ell)^{\rm w}_{ij} = \delta_{ij} \frac{C_{{\rm w},i}}{B^2_{\ell,i}}, \quad (24)$$

where $C_{{\rm w},i}$ is the map noise variance in band i and the Gaussian beam profile is

$$B^2_{\ell,i} \approx \exp\left[-\frac{\ell(\ell+1)}{8\ln 2}\theta^2_{{\rm FWHM},i}\right]. \quad (25)$$

In this case, the likelihood reduces to

$$-2\ln\mathcal{L} = \sum_{i,\ell} \frac{2\ell+1}{4\pi} \frac{B_{\ell,i}^2}{C_{\mathrm{w},i}} \left[\Delta T_{i,\ell} - y(\ell) T_0 g(x_i,\mu)\right]^2. \quad (26)$$

More generally we can include other noise terms, indexed by X, as additional contributions to the covariance matrix

$$(\mathbf{C}_\ell)_{ij} = (\mathbf{C}_\ell)_{ij}^{\mathrm{w}} + \sum_{\mathrm{X}} (\mathbf{C}_\ell)_{ij}^{\mathrm{X}} \quad (27)$$

and in particular for various foreground noise contributions that are fully correlated in frequency space, we take

$$(\mathbf{C}_\ell)_{ij}^{\mathrm{X}} = \sqrt{C_{\mathrm{X}}(\ell,\nu_i) C_{\mathrm{X}}(\ell,\nu_j)}, \quad (28)$$

where $C_{\mathrm{X}}(\ell,\nu_i)$ is the angular power spectrum of component X at frequency ν_i. We often characterize such contributions using their logarithmic power spectrum

$$D_{\mathrm{X}}(\ell,\nu_i) \equiv \frac{\ell(\ell+1)}{2\pi} C_{\mathrm{X}}(\ell,\nu_i). \quad (29)$$

To forecast measurement errors on μ we employ the Fisher matrix

$$\mathbf{F}_{\alpha\beta} = -\left\langle \frac{\partial^2 \ln\mathcal{L}}{\partial p_\alpha \partial p_\beta} \right\rangle, \quad (30)$$

where in our baseline study we take the parameters as $p_\mu \in y_c, \mu$ and evaluate the parameter derivatives around a fiducial model with $\mu = 0$ and the expected $y_c(M,z)$. We include T_e as a parameter when considering relativistic corrections in Sec. IV B. In general, the forecasted error on μ then comes from the $\mu\mu$ element of the matrix inverse of $\mathbf{F}$:

$$\sigma_k(\mu) = \sqrt{(\mathbf{F}^{-1})_{\mu\mu}}, \quad (31)$$

where k indexes the cluster so that the combined result of the independent clusters in the catalog is given by

$$\sigma^{-2}(\mu) = \sum_k \sigma_k^{-2}(\mu). \quad (32)$$

Since the sum over identical clusters involves the same σ_k, in practice we sum over mass and redshift bins that are narrow enough so as to provide results that is sufficiently close to the full sum once weighted by the expected number of clusters per bin.

IV. RESULTS

In this section, we present our main forecasting results. We begin by providing the forecasted constraints on μ for each of the three experimental configurations in the idealized or "baseline" case of white detector noise only. We then introduce real-world complexities that an experiment will have to address, including relativistic corrections to the tSZ effect, CMB background anisotropy, cluster-associated kinetic Sunyaev-Zeldovich (kSZ) signal, foreground sources, and atmospheric contamination. We report the degradation of constraints from each of these cumulatively. Since we do not analyze each effect separately, the ordering of the cumulative contributions can matter in the interpretation of which is seemingly the most significant. We choose this approach to instead emphasize which complexities, in descending order, are fundamental to the measurement and which ones are contaminants to specific experiments.

A. Baseline noise

Constraints on μ for each survey configuration for the baseline case of white detector noise only are shown in the first row of Table II. These represent the most optimistic possible projections from each survey and the baseline against which we compare the degraded constraints from successive real-world effects in the rest of the table and section.

We notice a few interesting results with regards to our baseline constraints on μ. For the two CMB-S4 surveys in this ideal forecast, $\sigma(\mu)$ is comparable to the bounds from COBE/FIRAS, which constrain $|\mu| < 9 \times 10^{-5}$ (95% C.L. [3]). With a CMB-HD-like configuration, we start to see improved constraints on μ relative to COBE/FIRAS, indicating that, from a raw sensitivity standpoint, this method of constraining μ has some promise.

In addition, we note that S4-deep provides a slightly better constraint on μ than S4-wide, despite the fact that the constraint comes from an order of magnitude fewer clusters. This can be understood from the fact that, for a fixed set of frequency bands, the per-cluster $\mu\mu$ Fisher matrix element [Eq. (31)] will scale as the square of the total signal to noise (S/N) on the tSZ signal from the cluster. In the ideal white-noise-only case, for the ith frequency channel and a cluster of a given mass and redshift, the squared, per-cluster tSZ S/N is given by

TABLE II. Forecasted constraint on μ for the baseline white detector noise of each experimental configuration and its cumulative degradation from additional effects.

$\sigma(\mu)$ assuming:	S4-wide	S4-deep	CMB-HD
Baseline noise only	1.6×10^{-4}	1.4×10^{-4}	2.8×10^{-5}
+ first-order rSZ	2.1×10^{-4}	1.9×10^{-4}	3.6×10^{-5}
+ CMB and background kSZ	2.5×10^{-4}	2.5×10^{-4}	4.4×10^{-5}
+ cluster kSZ	2.8×10^{-4}	2.6×10^{-4}	4.6×10^{-5}
+ extragalactic foregrounds	3.5×10^{-4}	7.0×10^{-4}	1.2×10^{-4}
+ galactic foregrounds	9.2×10^{-4}	9.1×10^{-4}	1.6×10^{-4}
+ atmosphere	1.3×10^{-3}	9.9×10^{-4}	1.9×10^{-4}

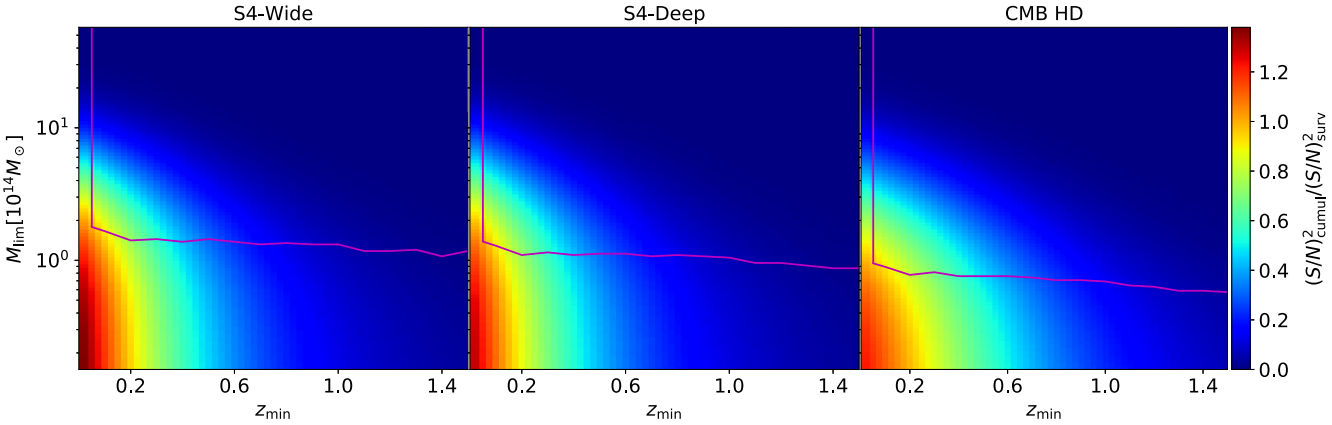

FIG. 3. The cumulative squared signal to noise, $(S/N)^2_{\rm cumul}$, above a given cluster mass and redshift threshold normalized to the total $(S/N)^2_{\rm surv}$ for the three surveys from their catalog of clusters with masses and redshifts above the red line.

$$\left(\frac{S}{N}\right)_i^2 = \sum_\ell \frac{2\ell+1}{4\pi}\frac{[y_\ell T_0 g(x_i,0)B_{\ell,i}]^2}{C_{{\rm w},i}} = \frac{[y_c T_0 g(x_i,0)]^2}{C_{{\rm w},i}}\sum_\ell \frac{2\ell+1}{4\pi}\left[2\pi\theta_c^2 K_0(\ell\theta_c)B_{\ell,i}\right]^2. \tag{33}$$

As expected, this scales as $y_c^2/C_{{\rm w},i}$.

The total μ constraint for a given survey will scale with this quantity summed over all the clusters in the catalog and frequency, $(S/N)^2_{\rm surv}$. For S4-wide $(S/N)^2_{\rm surv}$ is 1.5×10^9, for S4-deep it is 1.9×10^9, and for CMB-HD it is 2.3×10^{10}. The CMB-S4 wide survey covers 17 times more sky than the deep survey, so for any mass and redshift bin above the detection limit of both surveys, the wide survey will have 17 times more clusters in the catalog. But the square of the ratio of map noise in the main CMB bands in the two surveys—and, by extension the squared S/N per cluster—is over 20, so it is not surprising that the deep survey attains slightly better μ constraints.

This line of reasoning ignores the fact that the CMB-S4 deep survey also has a lower mass limit and a higher cluster number density, which in principle could lead to an even larger difference between the μ constraints from the deep and wide surveys. All of the clusters that will be in the S4-deep catalog but not the S4-wide catalog are low-mass systems with $z > z_{\rm min} = 0.05$, but as we shall see next, these clusters do not significantly improve the constraint.

To understand which clusters are providing most of the constraining power, we calculate the cumulative $(S/N)^2$ above a given mass and redshift and plot that quantity in Fig. 3. Specifically, we calculate the per-cluster $(S/N)^2$, calculated for frequency channel i using Eq. (33), sum over frequency channels and clusters above a given mass M and redshift z in the catalog, and plot this cumulative $(S/N)^2_{\rm cumul}(M,z)$.

Note that Fig. 3 extends the $(S/N)^2_{\rm cumul}$ to below our fiducial values for $M_{\rm lim}(z)$ and $z_{\rm min}$ (red lines) so that the ratio with the given survey $(S/N)^2_{\rm surv}$ can exceed unity. Nonetheless, in each case half of $(S/N)^2$ at $z_{\rm min}$ comes from cluster masses well above $M_{\rm lim}(z_{\rm min})$ and at $M_{\rm lim}(z)$ from cluster redshifts below $z < 0.5$. This implies that the clusters around $M_{\rm lim}(z)$ for each survey are not providing much constraining power on μ if $z_{\rm min} = 0.05$. It is only for $z < 0.05$ and masses substantially below $M_{\rm lim}(z_{\rm min})$ that the cumulative $(S/N)^2$ changes noticeably, but even then only by 20%—30%.[1]

In this work we produce forecasts for fixed instrument configurations, but it is possible that small modifications to one or more of the configurations could improve the μ constraints. In particular, it is not obvious from just the total S/N which frequency bands are contributing most to the constraint and where more bands could potentially help. We note that, when the frequency band allocation is not fixed, the total μ constraint depends not just on the total S/N but also includes the sensitivity of bands to the μ distortion. We can write the $\mu\mu$ Fisher matrix element as

$$\mathbf{F}_{\mu\mu} = \sum_i \left(\frac{S}{N}\right)_i^2 \left(\frac{\partial \ln g(x_i,\mu)}{\partial\mu}\right)^2, \tag{34}$$

where recall $\partial \ln g/\partial\mu$ is shown in Fig. 1. Of course, the final constraint on μ depends on the other contributions to the signal that must be marginalized over.

In the simple case where only y_c is marginalized over, we can build intuition for which frequencies contribute most to the μ constraint by considering the scenario with only two channels, in which case the squared uncertainty on μ (or,

[1]At least part of this signal could be recovered by augmenting the internal cluster catalogs with external detections in the optical and x-ray bands. For example, the cluster mass limit for the all-sky survey of the currently operating eROSITA mission is $\lesssim 2\times10^{13}M_\odot$ at $z < 0.1$ (see, e.g., Fig. 5.1.1 in [37]).

equivalently, the $\mu\mu$ element of the inverse Fisher matrix) is given analytically by

$$\sigma^2(\mu) = \frac{(S/N)_1^2 + (S/N)_2^2}{(S/N)_1^2 (S/N)_2^2} \left[\frac{\partial}{\partial\mu} \ln \frac{g(x_1,\mu)}{g(x_2,\mu)}\right]^{-2}. \quad (35)$$

From Eq. (35), it is clear that both sensitivity and frequency lever arm are important for constraining μ, as $\sigma^2(\mu)$ blows up when the S/N in either of the two bands gets too small or when $g(x,\mu)$ is similar enough between the bands that the spectral signature becomes indistinguishable from that of y_c. For estimation purposes, we find that the expression

$$\left(\frac{S}{N}\right)_i^2 \approx \frac{(y_c T_0)^2}{C_{\mathrm{w},i}} \frac{\pi\theta_c^2 g^2(x_i,0)}{1 + (\theta_{\mathrm{FWHM},i}/4\theta_c)^{1.6}} \quad (36)$$

approximates Eq. (33) to within a few percent for all clusters and instrument configurations discussed here. To further illuminate scaling results we can also roughly scale $\sqrt{C_\mathrm{w}}$ and θ_FWHM with frequency from 150 GHz to mimic CMB-S4 wide survey specifications:

$$\frac{\sqrt{C_\mathrm{w}}(\nu)}{2\ \mu\mathrm{K\text{-}arcmin}} = 1 + 11.5\left(\frac{\nu}{150\ \mathrm{GHz}} - 1\right)^2, \quad (37)$$

$$\frac{\theta_\mathrm{FWHM}(\nu)}{1.5\ \mathrm{arcmin}} = \left(\frac{\nu}{150\ \mathrm{GHz}}\right)^{-1}. \quad (38)$$

We plot Eq. (37) in Fig. 4 (upper panel, curve) and compare it against the actual CMB-S4 wide channel noise (points). Using this noise curve and Eq. (38), in Fig. 4 (bottom panel), we show $\sigma^2(\mu)$ for a cluster with $y_c = 1\times10^{-4}$ and $\theta_c = 1$ arcmin in this two-channel case, as a function of the frequency of the second channel ν with the first fixed at either $\nu_1 = 30$, 90, or 150 GHz.

Notice that $\sigma^2(\mu)$ diverges whenever the two frequencies have the same value of $\partial\ln(\Delta T)/\partial\mu$ (see Fig. 1), causing μ to become degenerate with y_c in the fit. This occurs by definition when the two frequencies are coincident, and, for a lower frequency ν_1 below the null, it occurs again for a specific upper frequency ν_2. In the limit where the lower frequency goes to zero and the μ response diverges, this second degeneracy between μ and y_c occurs when the upper frequency approaches the null. For a lower frequency around 150 GHz, the degeneracy disappears since the response in Fig. 1 is near the local minimum where it is single valued in frequency. The degeneracy is "accidental" in the sense that it only exists for pairs of frequency channels and is resolved once there are three or more channels. As we shall see next, the more complexity we add onto this baseline case the more multiple frequency channels are required to distinguish the μ signal.

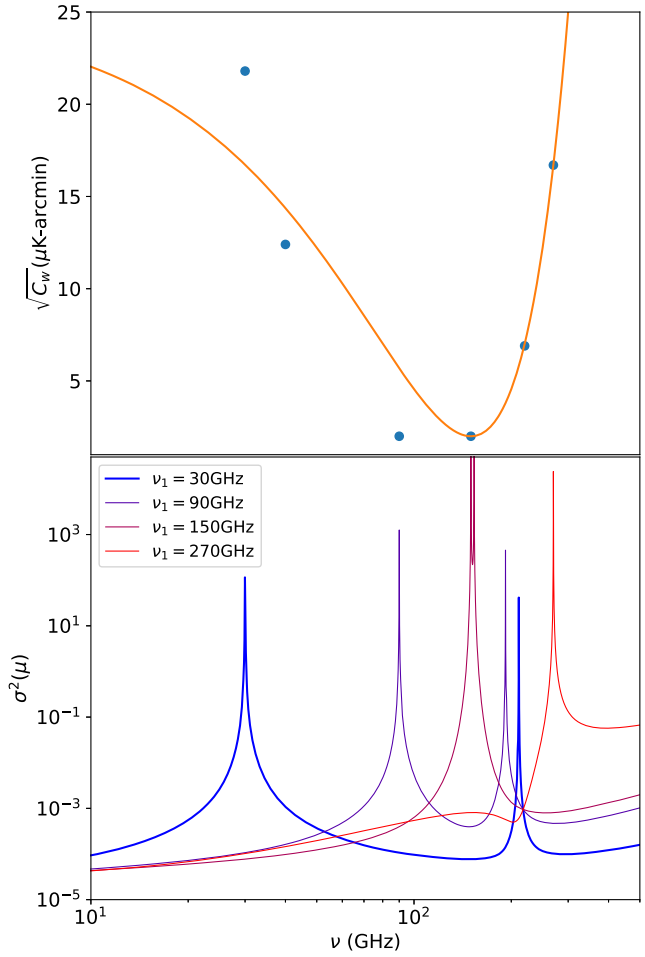

FIG. 4. Top: frequency scaling relation for $\sqrt{C_\mathrm{w}}$. Blue points correspond to the S4-wide survey's specifications. Bottom: $\sigma^2(\mu)$ for different frequency pairs for a single cluster with $y_c = 10^{-4}$ and $\theta_c = 1$ arcmin. We see that the constraints on μ improve when the channels are separated from each other rather than being closely spaced. In general, we see that as long as there is a separation, lower-frequency channels provide more sensitivity to μ in this baseline case of white detector noise only, in accordance with Fig. 1.

B. Relativistic corrections

So far when forecasting μ distortions from the distorted tSZ spectrum, we have used the nonrelativistic limit of the tSZ frequency spectrum. In reality, the hottest clusters, from which most of our constraining power is derived, are going to have non-negligible relativistic corrections, sometimes called the relativistic Sunyaev-Zeldovich (rSZ) effect, especially compared to the small level of distortion that μ introduces. We show in Appendix B that the μ-distorted rSZ spectrum modifies Eq. (12) for the anisotropy calibrated temperature fluctuation to

$$\Delta T = y T_0 g(x,\mu,\theta_e), \quad (39)$$

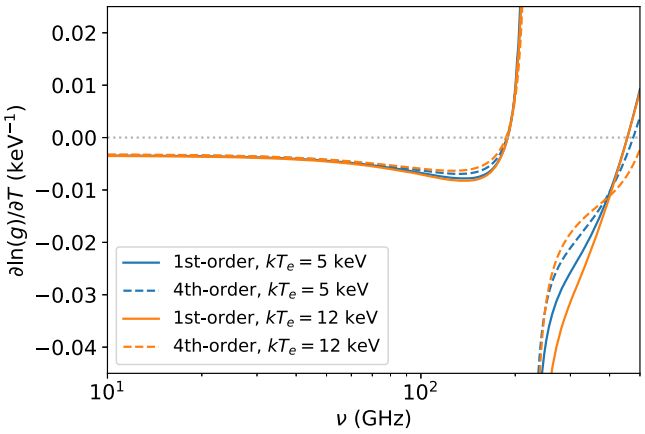

FIG. 5. The fractional response of the tSZ spectrum, with first-order and fourth-order relativistic corrections, to the temperature of the cluster. Here we take $\mu = 0$ for a cluster with $k_B T_e = 5$ keV and another with $k_B T_e = 12$ keV.

where $\theta_e = k_B T_e / m_e c^2$. This generalizes from the form $g(x, \mu, 0) = g(x, \mu)$ given in Eq. (4).

We then marginalize over T_e per cluster bin, around the central values given by Eq. (18), along with y_c using the first order in θ_e expression for g from Eq. (B3). In Fig. 5, we show the corresponding fractional change in the y distortion as a function of frequency for a range of cluster temperatures for comparison with Fig. 1 for the μ distortion. Marginalizing over T_e per cluster bin degrades our constraint on μ by ∼30% (see Table II). While this is not a large effect by itself, marginalizing over T_e has the effect of using up another linear combination of frequency bands to help break the degeneracy with μ, as was the case with y_c.

As noted by Ref. [38], the convergence of relativistic corrections as a Taylor expansion in powers of θ_e is slow at frequencies around the null and above. In Fig. 5, we also show the spectral shape of the relativistic correction at fourth order. The small change in the shape associated with the central frequencies of the surveys, which are below the null, implies a correspondingly small change in the μ constraints. We find that going to fourth order makes a 5% change for S4-wide, a 6% change for S4-deep, and a 3% change for CMB-HD.

C. CMB anisotropies

Another source of variance in the measurement of the tSZ effect from clusters is primary CMB anisotropy. As can be inferred from Fig. 3, the constraint on μ is dominated by high-mass, low-redshift clusters. These clusters are sufficiently extended on the sky that primary anisotropy is a potential concern.

There are also secondary CMB anisotropies arising from the kSZ effect due to scattering off of gas through its bulk rather than thermal motion after recombination. The kSZ effect is intrinsically a Doppler shift and has the same spectrum as primary anisotropies (see Sec. II B). In this section, we only consider the background kSZ signal rather than the contribution specific to the clusters in our catalog. The isotropic kSZ signal is subdominant relative to the primary CMB anisotropies until $\ell \gtrsim 4000$.

Since these sources are statistically isotropic, we model their effects on our constraints by including the CMB temperature power spectrum and kSZ power spectrum in our noise covariance matrix. As described in Sec. II A, the spectrum for CMB anisotropies will look like the derivative of a blackbody given that our experiments will calibrate off the anisotropies. Such sources have a constant temperature across frequencies by definition. This means that the temperature power spectra will act as frequency-independent, fully correlated noise across frequency channels in Eqs. (28) and (29). We use CAMB to generate the primary CMB logarithmic power spectrum $D_{TT}(\ell)$ for the fiducial cosmology. For the kSZ power spectrum, we consider a scale invariant spectrum with a constant $D_{\rm kSZ}(\ell)$. We use the amplitude measured from the South Pole Telescope (SPT) at $\ell = 3000$ [39], $D_{\rm kSZ}(3000) = 2.9\ \mu{\rm K}^2$.

As shown in Table II, $\sigma(\mu)$ slightly degrades when including the CMB and kSZ background, but not by a large amount. For both CMB-S4 surveys, the individual contribution of the CMB and kSZ effect are similar to one another. The smaller beams and wider ℓ coverage of CMB-HD make the kSZ effect relatively more important than the primary CMB.

D. Cluster kinetic Sunyaev-Zeldovich effect

In the previous section, we only considered the kSZ signal corresponding to a statistically isotropic background. Since each cluster also has a specific kSZ profile associated with its gas profile and peculiar motion, we cannot treat it as statistically isotropic noise as we can with foregrounds that are not associated with the cluster.

We could model the kSZ signature from each cluster as part of the cluster signal and marginalize over the peculiar velocity of the cluster as we did for y_c and T_e. On the other hand, the spectrum of the kSZ is perfectly known, and we can effectively marginalize over a signal with a known spectrum by adding a component with that spectrum and artificially high amplitude to the covariance matrix [40]. Since kSZ has the same spectrum as the primary CMB anisotropy, which already is in the covariance matrix with an amplitude much larger than the instrumental noise, we expect this procedure to have minimal impact on our μ constraints. In practice, we marginalize over any signal with the spectrum of primary CMB anisotropy or kSZ by multiplying the $D_{TT} + D_{\rm kSZ}$ spectra by a sufficiently large constant that the resulting $\sigma(\mu)$ saturates to its asymptotic value. Any part of the μ signal that comes from the combination of frequency channels with a blackbody spectrum will have effectively infinite noise and not contribute to the constraint.

The fourth row of Table II shows $\sigma(\mu)$ when we implement this procedure. We see that our constraints hardly change for all three CMB surveys. This suggests that, as expected, any contribution to the μ constraint from the combination of frequency band information corresponding to the spectrum of primary CMB anisotropy is already made negligible by the inclusion of the fiducial $D_{TT} + D_{\rm kSZ}$ in the covariance.

E. Extragalactic foregrounds

We treat three independent types of extragalactic foregrounds $X \in c, p, r$: "c" the clustered cosmic infrared background (CIB); "p" the spatially unclustered or "Poisson" component of the CIB; and "r" the radio sources or synchrotron-emitting active galactic nuclei, the clustering of which is assumed to be negligible. For extragalactic foregrounds and, in the next section, galactic foregrounds, we parametrize the logarithmic power spectrum of foreground X at multipole ℓ and frequency ν as

$$D_{\rm X}(\ell,\nu) \propto \left[\frac{f_{\rm X}(\nu)}{(\partial B/\partial T)_\nu}\right]^2 \ell^{\beta_{\rm X}} \tag{40}$$

and provide the normalization $D_{\rm X}(\ell_{\rm X},\nu_{\rm X})$ at a fiducial multipole value $\ell_{\rm X}$ and frequency $\nu_{\rm X}$. Here $\beta_{\rm X}$ is the index of the assumed power-law multipole dependence, $f_{\rm X}(\nu)$ encodes the frequency dependence in specific intensity units, and $(\partial B/\partial T)_\nu$ converts specific intensity to CMB temperature units at the relevant frequency ν assuming a blackbody CMB spectrum.[2] We assume 100% correlation between observing bands for all individual extragalactic and galactic foreground components, such that we only need to specify the behavior at a single frequency, with the cross-frequency components of the covariance given by Eq. (28).

For all three extragalactic foregrounds considered here, we assume a power-law frequency dependence

$$f_{\rm X}(\nu) = \nu^{\alpha_{\rm X}}. \tag{41}$$

Following [39], for the clustered CIB we adopt $D_{\rm c}(3000, 150\ {\rm GHz}) = 3.5\ \mu{\rm K}^2$ and $\alpha_{\rm c} = 4.3$, while for the Poisson component of the CIB we adopt $D_{\rm p}(3000, 150\ {\rm GHz}) = 9.2\ \mu{\rm K}^2$ and $\alpha_{\rm p} = 3.3$, and for the radio Poisson component, we adopt $D_{\rm r}(3000, 150\ {\rm GHz}) = 2.0 \times 10^{-2}\ \mu{\rm K}^2$ and $\alpha_{\rm r} = -0.70$. For the ℓ dependence, we adopt $\beta_{\rm c} = 0.80$ (again following [39]), while for the Poisson terms $\beta_{\rm p} = \beta_{\rm r} = 2$ by definition.

[2]Note that we neglect the μ-dependent anisotropy calibration C factors from Eq. (10) here, since we are considering the foregrounds as noise rather than signal. In principle, measuring anisotropy-calibrated foregrounds with known absolute spectra could themselves be used to measure μ.

We note that the assumed radio amplitude we adopt is significantly lower than the best-fit radio source power quoted in [41] (the follow-up paper to [39], which did not constrain the radio amplitude), owing to the assumption of a much lower source cut threshold in the experiments treated here. The 5σ point source threshold in the 150 GHz channel of the CMB-S4 deep survey should be roughly $50\times$ lower than that used in [41], and the slope of the number counts of radio sources is such that the Poisson power should scale roughly linearly with flux cut. As such, we adopt a radio amplitude value $50\times$ smaller than the $1.0\ \mu{\rm K}^2$ value from [41]. This number will be slightly optimistic for CMB-S4 wide and slightly pessimistic for CMB-HD.

We see in Table II that extragalactic foregrounds have a larger impact on our constraints of μ than the effects of the previous sections. Moreover CMB-HD no longer provides improvements on μ compared to the constraints from COBE/FIRAS. More specifically, in all three of our surveys, radio point sources are the dominant extragalactic foreground contaminating our constraints on μ. Both the clustered and Poisson contributions of the CIB have a negligible effect on $\sigma(\mu)$. Thus, efforts to reduce the effects of extragalactic foregrounds should prioritize mitigating the effects of radio sources. One clear path forward is to exploit the available lower-frequency data, both in the CMB surveys themselves and in planned contemporaneous radio surveys such as the Square Kilometer Array (SKA [42]), the source detection threshold of which will be such that masking of SKA-detected sources in CMB-S4 or CMB-HD data will be limited by the number of independent pixels or resolution elements in the map. Using current source models (e.g., [43]), the source density at flux cut levels a factor of several lower than those assumed here still only reaches hundreds per square degree, still feasible for masking in CMB-HD data.

Note that we are implicitly treating extragalactic foregrounds as a statistically isotropic background to the cluster signal. In fact, galaxy clusters will likely be overdensities of "foreground" contamination as well as the desired tSZ signal. A potential method to account for this would be to parametrize the covariance matrix with amplitude parameters for each extragalactic component and marginalize over these parameters per cluster. With sufficiently informative priors from observations in other surveys and at other wavelengths, this could be achieved with a minimal degradation of the eventual μ constraint.

F. Galactic foregrounds

The sources of galactic contamination that have traditionally been considered most important at CMB observing frequencies are thermal dust emission and synchrotron emission, but we also include a component of "anomalous microwave emission" (AME) because of its importance at low frequencies (e.g., [44]).

Because galactic foregrounds are not statistically isotropic, we adopt separate sets of values for foreground amplitudes for the $f_{\rm sky} = 0.03$ S4-deep survey and the $f_{\rm sky} = 0.5$ region targeted by the S4-wide survey (which we also adopt for the CMB-HD survey).[3]

Interstellar dust heated by starlight emits as a quasithermal modified blackbody. We follow Ref. [45] and parametrize the frequency behavior of thermal dust emission as

$$f_{\rm d}(\nu) = \nu^{\alpha_{\rm d}} B_\nu(T_{\rm d}), \tag{42}$$

where $T_{\rm d} = 19.6$ K is the dust temperature and $\alpha_{\rm d} = 1.6$. Also following that work, we set $\beta_{\rm d} = -0.4$. Following Ref. [46], we adopt $D_{\rm d}(80, 145\ {\rm GHz}) = 3.3\ \mu{\rm K}^2$ for S4-deep and $1.2 \times 10^3\ \mu{\rm K}^2$ for S4-wide and CMB-HD.[4] This very large increase from deep to wide is attributed at least partly to the requirement adopted in the CMB-S4 wide survey to restrict observing elevation to $\geq 40°$. If we impose no elevation restriction and instead choose the 50% of the sky at highest galactic latitude (using the publicly available PySM simulations [47] as in [46]), we find $D_{\rm d}(80, 145\ {\rm GHz}) = 63\ \mu{\rm K}^2$. This would similarly reduce the impact of AME on the wide surveys (see below for details).

Again following Ref. [45], we parametrize synchrotron as a pure power law in frequency [as in Eq. (41)] and adopt $\alpha_{\rm s} = -1.1$ and $\beta_{\rm s} = -0.4$. Likewise following Ref. [46], we adopt $D_{\rm s}(80, 93\ {\rm GHz}) = 5.0 \times 10^{-3}\ \mu{\rm K}^2$ for S4-deep and $5.5 \times 10^{-2}\ \mu{\rm K}^2$ for S4-wide and CMB-HD. We note that the synchrotron amplitude does not vary as strongly across the sky in PySM as the dust amplitude: The ratio of power in the wide and deep areas is only ~ 10 for synchrotron, compared to over 300 for dust. Similarly, if we use $|b| > 30°$ instead of the official CMB-S4 wide region, we find that the synchrotron amplitude decreases by less than a factor of 2 (compared to ~ 20 for dust).

Because of the potential importance of low-frequency information in our μ constraint, we also consider the impact of AME. We investigate the behavior of AME in the CMB-S4 3% sky region using PySM. We find that the AME spectral energy distribution (SED) has a double-peaked shape, which we parametrize as

$$f_{\rm a}^2(\nu) = e^{-[\ln(\nu/\nu_1)]^2/2\sigma_1^2} + A e^{-[\ln(\nu/\nu_2)]^2/2\sigma_2^2}, \tag{43}$$

with $\nu_1 = 10$ GHz, $\sigma_1 = 0.43$ GHz, $\nu_2 = 22$ GHz, $\sigma_2 = 0.35$ GHz, and $A = 6.5 \times 10^{-3}$. We assume $\beta_{\rm a} = -0.4$ (as would be expected if AME were from spinning dust grains and traced the thermal dust emission). From PySM, we estimate $D_{\rm a}(80, 10\ {\rm GHz}) = 1.0 \times 10^4\ \mu{\rm K}^2$ for the S4-deep survey and, assuming the same scaling between deep and wide found for the thermal dust, $D_{\rm a}(80, 10\ {\rm GHz}) = 3.6 \times 10^6\ \mu{\rm K}^2$ for S4-wide and CMB-HD.

The inclusion of galactic foregrounds has a larger impact on S4-wide compared to S4-deep and CMB-HD, which are more impacted by extragalactic than galactic foregrounds due to their μ constraint being weighted toward higher multipoles (see Table II). More specifically, S4-wide and S4-deep now have comparable constraints on μ, despite vastly different galactic foreground amplitudes. Most notably, AME is responsible for most of the degradation in $\sigma(\mu)$ for all three surveys. Synchrotron provides some contribution while being subdominant to AME, and dust has a negligible effect on $\sigma(\mu)$. As discussed above, relaxing restrictions on observing elevation in the wide surveys can help mitigate the impact of AME. But this result also motivates a more careful investigation into the spectral and spatial behavior of AME, beyond the simple ansatz made in this work.

We also note that, because of the large variation in galactic foreground amplitudes across the wide survey region, using a single covariance matrix for the wide-area surveys is almost certainly suboptimal. The true foreground covariance across the full region will have off-diagonal elements in ℓ space, owing to the statistical anisotropy across the region, but even including these off-diagonal elements, the use of a single covariance matrix implicitly assumes statistical isotropy across the field. Because of this, the constraints presented here for the wide surveys are likely somewhat pessimistic. We could potentially recover some of the μ constraints lost to galactic foregrounds (and make the use of covariance matrices that are diagonal in ℓ more appropriate) by dividing the wide surveys into subpatches based on foreground amplitude and analyzing each subpatch individually, with different covariance matrices. This would effectively weight different parts of the wide survey region inversely by foreground amplitude.

G. Atmosphere

We saw in our S/N contour plot that most of the signal is from high-mass, low-redshift clusters, and they can subtend a large angle in the sky. In addition to being potentially confused with primary CMB fluctuations (see Sec. IV C), signals from objects this large on the sky are also impacted (in ground-based measurements) by emission from poorly mixed water vapor in the atmosphere. The amplitude of water-vapor fluctuations in the atmosphere is higher at large spatial scales than small spatial scales, and the emission thus behaves as "red noise" in CMB maps, often modeled as a power law in ℓ. The total detector + atmosphere noise power in frequency band i can then be parametrized with three numbers, namely the white noise level $C_{\rm w}$, the multipole value at which the detector and

[3]Because of the statistically anisotropic nature of the galactic foregrounds, in a real dataset, the covariance for clusters in different parts of the sky would be potentially quite different, and using the mean covariance across the sky for all clusters is not strictly correct.

[4]This is technically for $f_{\rm sky} = 0.58$, but if we recalculate for $f_{\rm sky} = 0.50$, the value only decreases by $\sim 30\%$.

TABLE III. Atmosphere parameters for the CMB-S4 wide and deep surveys and a CMB-HD-like survey, taken from [32].

Channels (GHz)		30	40	90	150	220	270
Survey	$f_{\rm sky}$	$\ell_{\rm knee}$ and $\alpha_{\rm atmo}$					
S4-wide	50%	400	400	1900	3900	6700	6800
		3.5	3.5	3.5	3.5	3.5	3.5
S4-deep	3%	400	400	1200	1900	2100	2100
		4.2	4.2	4.2	4.1	4.1	3.9
CMB-HD	50%	400	400	1900	3900	6700	6800
		3.5	3.5	3.5	3.5	3.5	3.5

atmosphere noise levels are equal $\ell_{\rm knee}$, and the power-law index of the atmosphere noise $\alpha_{\rm atmo}$:

$$C_{{\rm w},i} \to C_{{\rm w},i}\left[1+\left(\frac{\ell_{{\rm knee},i}}{\ell}\right)^{\alpha_{{\rm atmo},i}}\right]. \tag{44}$$

Our values of $\ell_{\rm knee}$ and $\alpha_{\rm atmo}$ for the three surveys are taken from [32] and given in Table III.

While Eq. (44) describes atmospheric emission as uncorrelated between frequency bands, physical intuition and empirical evidence (e.g., [48]) argue that it should in fact be strongly correlated between bands, at least for instruments in which the beam patterns for detectors at different frequencies overlap in the atmosphere. The effects of atmosphere could in principle be reduced using the correlation between frequency bands to project out much of the atmospheric contamination.

H. Order of operations

Our chosen ordering of cumulative effects may give the impression that certain effects are negligible because they are when implemented early in the ordering. However, these effects could prove significant when implemented last, after the survey's constraining power is used to fix other effects. To help gauge the impact each effect has on the end result, we calculate $\sigma(\mu)$ when excluding individual effects from the end result. These results are shown in Table IV.

TABLE IV. Forecasted fractional improvement to $\sigma(\mu)$ (see last line of Table II for the values for each experimental configuration) when excluding certain individual effects.

Excluded	S4-wide	S4-deep	CMB-HD
First-order rSZ	×0.60	×0.58	×0.68
CMB and all kSZ	×0.90	×0.94	×0.97
Cluster kSZ	×0.97	×0.99	×0.98
Extragalactic foregrounds	×0.99	×0.79	×0.92
Galactic fore	×0.41	×0.83	×0.71

$\sigma(\mu)$ when excluding relativistic contributions, compared to including first-order corrections, improves by ∼40% for both CMB-S4 surveys, whereas the results improve by ∼30% for CMB-HD. If we include the effect up to fourth order, the results are almost identical to first-order results.

The CMB and the kSZ effect, both the isotropic and cluster component, have a negligible impact on $\sigma(\mu)$ when excluded at the end. Interestingly, extragalactic foregrounds also have a negligible impact on μ for S4-wide and CMB-HD. S4-deep's constraint improves when we exclude extragalactic foregrounds but only by about 25%.

The exclusion of galactic foregrounds improves S4-wide and CMB-HD's constraints on μ but only modestly improves S4-deep's constraints. This is likely because contamination from galactic foregrounds is much worse for S4-wide and CMB-HD, which include observations near the galactic plane.

Our results suggest that the largest way to improve constraints on μ for all surveys is to address relativistic corrections. For S4-wide and CMB-HD, galactic foregrounds are a major challenge to improving constraints. For S4-deep, galactic and extragalactic foregrounds present similar levels of degradation. Generally, addressing these challenges requires additional frequency channels in order to help isolate the μ signal. Finally, we note that priors on T_e can in principle be obtained from external data such as x-ray observations.

I. Interfrequency calibration requirement

While we can effectively perfectly account for the miscalibration induced from assuming the background photon distribution is a blackbody when it is in fact a Bose-Einstein distribution, in a real instrument there will also be miscalibration from the fact that the observation of the calibration source is not noise-free. If we parametrize this calibration error as

$$C_{\rm meas} = C_{\rm true}(1+\delta_{\rm cal}) \equiv 1+\delta_{\rm cal}, \tag{45}$$

then in a real experiment, the measured, (mis)calibrated signal from a single cluster will be

$$\Delta T(x, y_c, \mu, \delta_{\rm cal}) = yT_0 g(x,\mu)(1+\delta_{\rm cal}). \tag{46}$$

The requirement for interfrequency calibration is most obvious in the Rayleigh-Jeans limit (and in the limit $\mu \ll x$), in which $g(x,\mu) = -2(1+\mu/x)$. The basic information used to constrain μ is the ratio of the cluster signal in two bands. If we assume perfect calibration in one band and a miscalibration in the other, we find

$$R(x_1, x_2, y_c, \mu, \delta_{\rm cal}) = \frac{\Delta T(x_2, y_c, \mu, \delta_{\rm cal})}{\Delta T(x_1, y_c, \mu)} = \frac{-2y_c T_0(1+\mu/x_2)(1+\delta_{\rm cal})}{-2y_c T_0(1+\mu/x_1)} = \frac{1+\delta_{\rm cal}+\mu/x_2+\delta_{\rm cal}\mu/x_2}{1+\mu/x_1} \simeq \left(1+\delta_{\rm cal}+\frac{\mu}{x_2}\right)\left(1-\frac{\mu}{x_1}\right) \simeq 1+\mu\left(\frac{1}{x_2}-\frac{1}{x_1}\right)+\delta_{\rm cal}. \quad (47)$$

It is clear from this formulation that to constrain μ to some level $\sigma(\mu)$, we need calibration uncertainty smaller than $\sigma(\mu)|(x_2^{-1}-x_1^{-1})|$. For the experimental configurations considered in this work, that means we need calibration better than 10^{-4}–10^{-5} in the bands around the peak of the CMB blackbody. A full-sky experiment with noise levels of 1 μK-arcmin has S/N per band on the primary CMB temperature anisotropy approaching 10^6, so in principle this level of interfrequency calibration is achievable.

Additionally, this level of calibration precision must be maintained over the full survey area. For surveys that cover a large fraction of the sky, different parts of the survey are in general surveyed at widely separated times and possibly under different atmospheric conditions. This places an effective requirement on calibration stability; alternatively, different parts of the survey can be calibrated independently, in which case the S/N requirement on the CMB is per independently calibrated patch.

Finally, we note that this calibration requirement imposes a practical minimum size of the survey area. Figure 3, taken at face value, implies that an efficient strategy for constraining μ with tSZ could be to make incredibly deep measurements on a single very massive and low-redshift cluster (or a handful of such clusters). If, however, the calibration for such a survey is to come from CMB anisotropy, the survey must contain enough sky in which the signal is dominated by primary CMB to achieve the required calibration precision. This disfavors strategies along the lines of pointing a powerful interferometer (such as ALMA) at a small number of massive clusters.

J. Cluster profiles

The model for the angular distribution of the Compton-y signal adopted in Sec. III is an oversimplification in at least three ways.

(1) Real clusters of the same mass and redshift will not all have the same overall normalization to their Compton-y signal.
(2) Real clusters of the same mass and redshift will not all have the same profile shape.
(3) The Compton-y signal in real clusters will not be described perfectly by an isothermal β-model profile.
(4) Real clusters are not spherically symmetric.

One important point to remember here is that, in our forecasting, the cluster model serves effectively as a weighting of angular modes, and getting this weighting wrong will result in a lower S/N and thus a worse constraint on μ but will not bias the result.

The impact of the first two effects, scatter in the overall normalization and profile shape at fixed mass and redshift, can be estimated using the expression in Eq. (33). In a given mass and redshift bin, if there is scatter in overall normalization or scale radius, but they are treated as uniform—for example, if the analysis is performed on a stacked cluster profile—the total achieved $(S/N)^2$ in a bin will be equal to $N_{\rm cl}(S/N)^2_{\rm mean}$, where $N_{\rm cl}$ is the number of clusters in the bin and $(S/N)^2_{\rm mean}$ is the result of Eq. (33) using the mean normalization or scale radius in the bin. The maximum achievable $(S/N)^2$, if each cluster was treated individually and its properties fully known, would be $\sum_i (S/N)^2_i$, and the degradation in $(S/N)^2$ from stacking is the ratio of these, $N_{\rm cl}(S/N)^2_{\rm mean}/\sum_i (S/N)^2_i$. Because the constraint on μ scales as the inverse square root of this quantity [i.e., $\sigma^2(\mu) = F^{-1}_{\mu\mu} \propto (S/N)^2$], the degradation on $\sigma(\mu)$ will be 1/2 the degradation on $(S/N)^2$ (for small degradation factors).

We estimate the degradation factor for 10% scatter in overall normalization (roughly the upper limit to the intrinsic scatter in the $Y-M$ relation found in [49]) and for 30% scatter in scale radius (see Table A2 in [28]). The effect of scatter in the normalization can be estimated analytically and should result in a degradation of order $\sigma^2_{y_0}/{y_0}^2$ in total $(S/N)^2$, or $0.5\sigma^2_{y_0}/{y_0}^2$ in σ_μ. This relation predicts a 1% degradation in total $(S/N)^2$ or 0.5% in $\sigma(\mu)$ for 10% scatter, and we find results consistent with this using Eq. (33) for a Gaussian distribution with $\sigma_{y_0}/y_0 = 0.1$. For a Gaussian distribution of scale radii with $\sigma_{\theta_c}/\theta_c = 0.3$, we find a degradation of roughly 10% in total $(S/N)^2$ or 5% in $\sigma(\mu)$.

Assuming the wrong cluster model or assuming a spherically symmetric cluster when the true cluster is elliptical or triaxial will result in a degradation in S/N even with no scatter in cluster shape within a mass and redshift bin. For a fiducial cluster with mass $M_{500} = 5\times10^{14}M_\odot$ and redshift $z = 0.5$, if we assume the true underlying profile is the universal pressure profile from [28], but we use a β model in the fitting procedure, we incur a penalty in $(S/N)^2$ of roughly 3%. If we assume the true underlying model is a β model with typical ellipticity (defined as ratio of minor to major axis) of 0.8 (cf. Table 2 in [50]), we find a degradation in $(S/N)^2$ of roughly 1%. All of these effects are small compared to the impact of the configuration choices described earlier and shown in Table II.

V. CONCLUSION

In this study, we have demonstrated that the spectrum of the tSZ effect in the direction of massive clusters of galaxies can be used to constrain the μ-distortion monopole. We have shown that this can in principle be achieved without measuring the mean intensity across the sky and instead using a differential experiment that calibrates off of the CMB anisotropies, even when assuming the underlying CMB is an undistorted blackbody. We forecasted constraints on μ using the tSZ spectrum for the upcoming CMB-S4 experiment, using both the wide and deep surveys, as well as the proposed CMB-HD experiment. We found that the most massive clusters at the lowest redshifts provide the strongest constraints on the μ-distortion monopole. In terms of raw sensitivity, we found that all three surveys closely match or outperform COBE/FIRAS in constraining the μ-distortion monopole. Extragalactic and galactic foregrounds significantly degrade these constraints to the point where CMB-S4 performs worse than COBE/FIRAS, and CMB-HD delivers roughly equivalent constraints to COBE/FIRAS. Specifically, we found that radio point sources heavily impact low-noise surveys such as S4-deep and CMB-HD, whereas the inclusion of AME significantly degrades S4-wide constraints on μ.

To improve on these constraints, foreground removal is a priority. Improving foreground removal, in general, requires additional frequency channels to help distinguish signal from foregrounds. In regards to specific foregrounds, improved masking of radio point sources using higher-resolution surveys should reduce their impact, while to reduce the effects of galactic foregrounds such as AME, the most straightforward strategy is to perform deep sky observations that avoid the galactic plane. We see in Figs. 1 and 4 that the distortion of the tSZ spectrum increases at lower frequencies. This suggests additional coverage at low frequencies should also improve constraints on μ. Finally, the inclusion of external data (particularly x-ray data) could be useful both in filling in the low-redshift gaps in the CMB experiments' cluster selection and in providing external priors on the temperature of individual clusters, helping to break degeneracies between μ, central tSZ decrement, and cluster temperature.

Based on the above discussion, an experiment that would improve on these current constraints should have many frequency channels to remove foregrounds, with some channels dedicated to frequencies below 30 GHz if possible. The experiment should have beams comparable to the targeted cluster sample with white noise levels comparable to or better than CMB-S4. This implies observations with radio instruments combined with a CMB experiment have the potential to improve measurements of μ. While our results suggest a deep observation of individual low-redshift clusters would be ideal for obtaining better constraints on μ, we caution that one would need to also measure in the same observation the CMB at a high enough SNR for all frequencies to calibrate off of CMB anisotropy.

Certain assumptions we make in our forecasts may turn out to be overly optimistic. For example, the assumption of 100% correlation between the foreground power across all frequency bands must break down at some level. Although the level of decorrelation in galactic dust at these frequencies has been limited to be very small [51], even a low level of decorrelation could degrade precision constraints significantly. On the other hand, analyzing the foregrounds in subpatches should improve the statistical modeling and more optimally weight the data. We also show that the degradation in $\sigma(\mu)$ due to scatter in the overall normalization and cluster shape is small compared to other effects we model. Although it is small, this degradation could be recovered in future work by fitting the true profile to each cluster in order to recover the maximum achieved $(S/N)^2$.

The low-frequency enhancement of μ distortions of the tSZ effect suggests that a synergistic combination of CMB and radio telescope data could further improve constraints on the μ monopole using this technique. To realize this promise with specific radio surveys, future studies can use the forecasting framework presented here to address the calibration and foreground-mitigation requirements of the combined dataset.

ACKNOWLEDGMENTS

We thank Andrey Kravtsov for useful conversations. D. Z. was supported by the National Science Foundation Graduate Research Fellowship Program under Grant No. DGE1746045. W. H. was supported by U.S. Department of Energy Contract No. DE-FG02-13ER41958 and the Simons Foundation. T. C. acknowledges support from National Science Foundation Grant No. OPP-1852617.

APPENDIX A: FLAT SKY HARMONICS

For a function on the sky $y(\vec{n} = \{\theta, \phi\})$ with support only on a small area $\theta \ll 1$ around the pole (in the main text, center of the cluster), we can directly relate the spherical harmonic $y_{\ell m}$ and flat sky y_ℓ harmonic coefficients

$$y(\vec{n}) = \sum_{\ell m} y_{\ell m} Y_{\ell m}(\vec{n}) \approx \int \frac{d^2\ell}{(2\pi)^2} y(\vec{\ell}) e^{i\vec{n}\cdot\vec{\ell}}, \tag{A1}$$

using an approximation for $Y_{\ell m}$ itself in an elaboration of the derivation in Ref. [52]. This approximation follows from the relation ([53], 8.722.2)

$$\ell^m P_\ell^{-m}(\cos\theta) \approx J_m(\ell\theta) \tag{A2}$$

for $m \geq 0$ and $\ell \gg 1$. We can use the fact that

$$J_{-m}(x) = (-1)^m J_m(x), \tag{A3}$$

$$P_\ell^{-m} = (-1)^m \frac{(\ell - m)!}{(\ell + m)!} P_\ell^m, \tag{A4}$$

and

$$Y_{\ell m} = \sqrt{\frac{2\ell + 1}{4\pi} \frac{(\ell - m)!}{(\ell + m)!}} P_\ell^m(\cos\theta) e^{im\phi} \tag{A5}$$

to obtain for all m

$$Y_{\ell m} \approx \ell^{-|m|} \sqrt{\frac{(\ell + |m|)!}{(\ell - |m|)!}} (-1)^m \sqrt{\frac{2\ell + 1}{4\pi}} J_m(\ell\theta) e^{im\phi}. \tag{A6}$$

When transforming functions with support only near the pole only $|m| \ll \ell$ modes contribute substantially due to the rapid variation of higher modes with ϕ, so it is a good approximation to cancel the factorials with $\ell^{-|m|}$ and use

$$Y_{\ell m} \approx (-1)^m \sqrt{\frac{2\ell + 1}{4\pi}} J_m(\ell\theta) e^{im\phi} \quad (|m| \ll \ell). \tag{A7}$$

Note that we can always orient the pole of the spherical coordinate system to align with the region of support. We can now obtain the desired relation between the two coefficients in Eq. (A1) [52]:

$$y(\vec{\ell}) \approx \sqrt{\frac{4\pi}{2\ell + 1}} \sum_m i^{-m} y_{\ell m} e^{im\varphi_\ell},$$
$$y_{\ell m} \approx \sqrt{\frac{2\ell + 1}{4\pi}} \int \frac{d\varphi_\ell}{2\pi} e^{-im\varphi_\ell} y(\vec{\ell}), \tag{A8}$$

where φ_ℓ is the azimuthal angle ϕ that $\vec{\ell}$ points at the pole. In particular, if the function is azimuthally symmetric around the pole only $m = 0$ coefficients contribute and

$$y(\vec{\ell}) = 2\pi \int \theta d\theta J_0(\ell\theta) y(\theta) \approx \sqrt{\frac{4\pi}{2\ell + 1}} y_{\ell 0}. \tag{A9}$$

It is common in the literature to slightly improve on the accuracy of the underlying approximation (A2) at low ℓ by taking the argument of the Bessel function as $\ell\theta \to (\ell + 1/2)\theta$ and correspondingly $\ell^2 \to \ell(\ell + 1)$, e.g., in the Gaussian beam profile formula (25).

APPENDIX B: RELATIVISTIC CORRECTIONS

Following Refs. [38,54], we can derive the relativistic corrections to the y distortion of an initial μ distortion using the generalized Kompaneets equation which is the expansion of the Compton collision term to the Boltzmann equation in the small energy transfer due to scattering. To first order in $\theta_e \equiv k_B T_e / m_e c^2$, Eq. (1) is generalized to

$$\frac{\partial f}{\partial \tau} = \theta_e \sum_{n=1}^{4} x_e^n I_n \left[(1 + f) \left(\frac{\partial}{\partial x_e} + 1 \right)^n - \frac{\partial^n f}{\partial x_e^n} \right] f \tag{B1}$$

with

$$I_1 = 4 - x_e + \left(10 - \frac{47}{2} x_e + \frac{21}{5} x_e^2 \right) \theta_e,$$
$$I_2 = 1 + \left(\frac{47}{2} - \frac{63}{5} x_e + \frac{7}{10} x_e^2 \right) \theta_e,$$
$$I_3 = \left(\frac{42}{5} - \frac{7}{5} x_e \right) \theta_e,$$
$$I_4 = \frac{7}{10} \theta_e. \tag{B2}$$

We can again find the change Δf in the $|y| \ll 1$ regime by plugging in an initial Bose-Einstein distribution to the right-hand side of Eq. (B1) to obtain $\Delta f = y x e^{x+\mu} f^2 g$, where

$$g = X - 4 + \theta_e \left[-10 + \frac{47}{2} X - \frac{42}{5} X^2 + \frac{7}{10} X^3 + S^2 \left(-\frac{21}{5} + \frac{7}{5} X \right) + \frac{7x^2}{10} (6 - X) \frac{T}{T_e} \right] \tag{B3}$$

and

$$X = x \coth[(x + \mu)/2], \qquad S = x \operatorname{csch}[(x + \mu)/2]. \tag{B4}$$

Recall that the Comptonization parameter y was defined in Eq. (5) to vanish for $T = T_e$.

For the tSZ effect in clusters where $T_e \gg T$, the expression becomes even simpler, reproducing and generalizing the $\mu = 0$ result found in Ref. [38]. This same rule for generalizing g in the presence of μ through the modification to X and S in Eq. (B4) applies to the higher order in θ_e terms of Ref. [38] for $T_e \gg T$ as we have explicitly checked to fourth order.

[1] C. L. Bennett *et al.* (WMAP Collaboration), Astrophys. J. Suppl. Ser. **208**, 20 (2013).
[2] N. Aghanim *et al.* (Planck Collaboration), Astron. Astrophys. **641**, A1 (2020).
[3] D. J. Fixsen, E. S. Cheng, J. M. Gales, J. C. Mather, R. A. Shafer, and E. L. Wright, Astrophys. J. **473**, 576 (1996).
[4] M. Gervasi, M. Zannoni, A. Tartari, G. Boella, and G. Sironi, Astrophys. J. **688**, 24 (2008).
[5] F. Bianchini and G. Fabbian, Phys. Rev. D **106**, 063527 (2022).
[6] R. A. Sunyaev and Y. B. Zeldovich, Astrophys. Space Sci. **7**, 3 (1970).
[7] R. A. Daly, Astrophys. J. **371**, 14 (1991).
[8] W. Hu, D. Scott, and J. Silk, Astrophys. J. Lett. **430**, L5 (1994).
[9] J. Chluba, R. Khatri, and R. A. Sunyaev, Mon. Not. R. Astron. Soc. **425**, 1129 (2012).
[10] B. Bolliet, J. Chluba, and R. Battye, Mon. Not. R. Astron. Soc. **507**, 3148 (2021).
[11] D. Zegeye, K. Inomata, and W. Hu, Phys. Rev. D **105**, 103535 (2022).
[12] S. K. Acharya and R. Khatri, J. Cosmol. Astropart. Phys. 02 (2020) 010.
[13] A. Ota, T. Takahashi, H. Tashiro, and M. Yamaguchi, J. Cosmol. Astropart. Phys. 10 (2014) 029.
[14] S. Mukherjee, J. Silk, and B. D. Wandelt, Mon. Not. R. Astron. Soc. **477**, 4473 (2018).
[15] S. Mukherjee, J. Silk, and B. D. Wandelt, Phys. Rev. D **100**, 103508 (2019).
[16] S. A. Balashev, E. E. Kholupenko, J. Chluba, A. V. Ivanchik, and D. A. Varshalovich, Astrophys. J. **810**, 131 (2015).
[17] Y. Rephaeli, Astrophys. J. **241**, 858 (1980).
[18] G. Luzzi, E. D'Angelo, H. Bourdin, F. De Luca, P. Mazzotta, F. Oppizzi, and G. Polenta, EPJ Web Conf. **257**, 00028 (2022).
[19] G. De Zotti, M. Negrello, G. Castex, A. Lapi, and M. Bonato, J. Cosmol. Astropart. Phys. 03 (2016) 047.
[20] E. L. Wright, in *Early Evolution of the Universe and its Present Structure*, edited by G. O. Abell and G. Chincarini (Cambridge University Press, Cambridge, 1983), Vol. 104, pp. 113–116.
[21] E. E. Kholupenko, S. A. Balashev, A. V. Ivanchik, and D. A. Varshalovich, Mon. Not. R. Astron. Soc. **446**, 3593 (2015).
[22] K. Abazajian *et al.*, Bull. Am. Astron. Soc. **51**, 209 (2019).
[23] S. Aiola *et al.* (CMB-HD Collaboration), arXiv:2203.05728.
[24] A. S. Kompaneets, Sov. J. Exp. Theor. Phys. **4**, 730 (1957).
[25] L. E. Bleem *et al.* (SPT Collaboration), Astrophys. J. Suppl. Ser. **216**, 27 (2015).
[26] T. Plagge *et al.*, Astrophys. J. **716**, 1118 (2010).
[27] J. Liu *et al.*, Mon. Not. R. Astron. Soc. **448**, 2085 (2015).
[28] M. Arnaud, G. W. Pratt, R. Piffaretti, H. Boehringer, J. H. Croston, and E. Pointecouteau, Astron. Astrophys. **517**, A92 (2010).
[29] M. Hasselfield *et al.*, J. Cosmol. Astropart. Phys. 07 (2013) 008.
[30] D. Nagai, A. V. Kravtsov, and A. Vikhlinin, Astrophys. J. **668**, 1 (2007).
[31] M. Arnaud, E. Pointecouteau, and G. W. Pratt, Astron. Astrophys. **441**, 893 (2005).
[32] S. Raghunathan, Astrophys. J. **928**, 16 (2022).
[33] S. Raghunathan, N. Whitehorn, M. A. Alvarez, H. Aung, N. Battaglia, G. P. Holder, D. Nagai, E. Pierpaoli, C. L. Reichardt, and J. D. Vieira, Astrophys. J. **926**, 172 (2022).
[34] J. L. Tinker, A. V. Kravtsov, A. Klypin, K. Abazajian, M. S. Warren, G. Yepes, S. Gottlober, and D. E. Holz, Astrophys. J. **688**, 709 (2008).
[35] http://www.benediktdiemer.com/code/colossus/.
[36] B. Diemer, Astrophys. J. Suppl. Ser. **239**, 35 (2018).
[37] A. Merloni *et al.* (eROSITA Collaboration), arXiv:1209.3114.
[38] N. Itoh, Y. Kohyama, and S. Nozawa, Astrophys. J. **502**, 7 (1998).
[39] E. M. George *et al.*, Astrophys. J. **799**, 177 (2015).
[40] J. R. Bond, A. H. Jaffe, and L. Knox, Phys. Rev. D **57**, 2117 (1998).
[41] C. L. Reichardt *et al.* (SPT Collaboration), Astrophys. J. **908**, 199 (2021).
[42] A. Weltman *et al.*, Pub. Astron. Soc. Aust. **37**, e002 (2020).
[43] G. De Zotti, R. Ricci, D. Mesa, L. Silva, P. Mazzotta, L. Toffolatti, and J. Gonzalez-Nuevo, Astron. Astrophys. **431**, 893 (2005).
[44] C. Dickinson *et al.*, New Astron. Rev. **80**, 1 (2018).
[45] K. Abazajian *et al.* (CMB-S4 Collaboration), Astrophys. J. **926**, 54 (2022).
[46] K. R. Dibert *et al.*, Phys. Rev. D **106**, 063502 (2022).
[47] B. Thorne, J. Dunkley, D. Alonso, and S. Naess, Mon. Not. R. Astron. Soc. **469**, 2821 (2017).
[48] W. L. Holzapfel, T. M. Wilbanks, P. A. R. Ade, S. E. Church, M. L. Fischer, P. D. Mauskopf, D. E. Osgood, and A. E. Lange, Astrophys. J. **479**, 17 (1997).
[49] P. M. Motl, E. J. Hallman, J. O. Burns, and M. L. Norman, Astrophys. J. Lett. **623**, L63 (2005).
[50] R. Piffaretti, P. Jetzer, and S. Schindler, Astron. Astrophys. **398**, 41 (2003).
[51] C. Sheehy and A. Slosar, Phys. Rev. D **97**, 043522 (2018).
[52] W. Hu, Phys. Rev. D **62**, 043007 (2000).
[53] I. S. Gradshteyn and I. M. Ryzhik, *Table of Integrals, Series and Products* (Academic Press, Cambridge, Massachusetts, 1994).
[54] A. D. Challinor and A. N. Lasenby, Astrophys. J. **499**, 1 (1998).